CORONAL VELOCITY MEASUREMENTS WITH ULYSSES: MULTI-LINK CORRELATION STUDIES DURING TWO SUPERIOR CONJUNCTIONS

P. JANARDHAN[1*], M. K. BIRD[1], P. EDENHOFEN[2], R. WOHLMUTH[2],
D. PLETTEMEIER[2], S. W. ASMAR[3], M. PÄTZOLD[4] and J. KARL[4]
[1]*Radioastronomisches Institut, Auf dem Hügel 71, 53121 Bonn, Germany*
[2]*Institut für HF-Technik, Universität Bochum, 44780 Bochum, Germany*
[3]*Jet Propulsion Lab., Calif. Inst. of Tech., Pasadena, CA 91109, U.S.A.*
[4]*Institut für Geophysik, Universität Köln, 50923 Köln, Germany*

(Received 19 December 1997; accepted 24 August 1998)

Abstract. A well-known method for studying the solar wind very close to the Sun (heliocentric distances: 4 to 40 solar radii) is by radio sounding between a spacecraft at superior conjunction and the Earth. The *Ulysses* Solar Corona Experiment was performed at the spacecraft's two solar conjunctions in summer 1991 and winter 1995, during which dual-frequency ranging and Doppler observations were conducted globally on a nearly continuous basis at the NASA Deep Space Network and other ground stations. The dual-frequency Doppler measurements were used to determine coronal plasma velocities by a cross-correlation analysis during those occasions when tracking data were recorded simultaneously at two well-separated ground stations. A 'filtering' technique was developed to suppress noise and enhance the 2-station correlations, a procedure particularly effective at small solar offsets. From the electron content measurements during the two solar conjunctions it was found that regions of higher electron density tend to occur when the two-station correlations yield slower outward flow velocities.

1. Introduction

Several techniques have been developed in the past four or five decades for observing the solar corona and the solar wind. Using a variety of *in situ* and remote-sensing techniques to study the solar wind, variations in the structure and dynamics of the solar wind plasma have been observed on time scales from several minutes to the rotation period of the Sun and on up to the 11 and 22-year periods of the solar activity and magnetic cycles, respectively. Recent reviews of the techniques used and the knowledge gained have been written by Jackson (1991), Bird and Edenhofer (1990), and Schwenn (1990). Most of these techniques are applicable to the study of the solar wind either close to the Sun (heliocentric distances $r < 40\ R_\odot$, where $R_\odot$ = solar radius) or close to the Earth ($r \simeq 215\ R_\odot$).

The earliest ground-based observations of the solar corona and the solar wind (e.g., Hewish and Wyndham, 1963; Hewish, Scott, and Wills, 1964; Dennison

* Humboldt fellow: on Leave from the Physical Research Laboratory, Ahmedabad 380 009, India.

Solar Physics **184:** 157–172, 1999.

and Hewish, 1967; Hewish and Symonds, 1969; Coles and Maagoe, 1972; Kakinuma, Washimi, and Kojima, 1973) exploited the phenomenon of interplanetary scintillations (IPS) at meter wavelengths, and IPS observations have continued to the present day (e.g., Rickett and Coles, 1991; Manoharan *et al.*, 1995; Ananthakrishnan, Balasubramanian, and Janardhan, 1995; Janardhan *et al.*, 1996). IPS still remains the only ground-based method for studying the large-scale properties of the solar wind in the distance range 40 $R_\odot \leq r \leq 215\ R_\odot$. With the advent of spacecraft, however, it became possible to investigate the solar wind much closer to the Sun (e.g., Yakovlev *et al.*, 1980; Efimov *et al.*, 1981; Woo and Armstrong, 1981; Tyler *et al.*, 1981; Woo *et al.*, 1982) using radio links between deep space probes and the Earth. Such observations are rare as they require the fortuitous placement of a spacecraft in superior conjunction and are generally confined to the ecliptic plane.

The *Ulysses* spacecraft, the first to leave the ecliptic plane and orbit the Sun in a polar orbit, underwent two solar conjunctions (referred to as C_1, and C_4) in summer 1991 and winter 1995, respectively. Extensive dual-frequency (S- and X-band) ranging and Doppler observations were conducted in support of the *Ulysses* Solar Corona Experiment (SCE) during these conjunctions. The spacecraft was tracked globally on a nearly continuous basis by the NASA Deep Space Network (DSN) of telescopes and other ground stations in Europe (Bird *et al.*, 1992). While the ray path from *Ulysses* to Earth was always close to the ecliptic during the conjunction in August–September 1991 (Pätzold *et al.*, 1992; Bird *et al.*, 1994), it passed through all heliolatitudes from South Pole to equator at distances between 20–30 $R_\odot$ during the conjunction in February–March 1995 (Pätzold *et al.*, 1995; Bird *et al.*, 1996). This work presents the results of a two-station cross-correlation analysis of dual-frequency Doppler measurements to determine coronal plasma velocities during both C_1 and C_4.

2. Velocity Measurements from Two-Station Cross Correlations

Radio waves passing through an ionized medium experience a change in their phase and group velocities as compared with their free-space values. This phenomenon can be used to investigate the solar corona using radio links between the Earth and a spacecraft near superior conjunction (Bird, 1982). The radio subsystem configuration for the *Ulysses* SCE consists of an S-band uplink and a dual-frequency S/X-band downlink, both of which are phase coherent with the uplink. The downlink frequencies are $f_s = 2.293$ GHz and $f_x = 8.408$ GHz (fixed ratio $f_x/f_s = \frac{11}{3}$). The variation in the phase velocity due to changes in the density of the intervening plasma results in a frequency-dependent Doppler shift of the two received carrier frequencies. The plasma-induced variations can be isolated from nondispersive effects by calculating an observable called the ‘differential Doppler residual’

$$\delta f_{sx} = f_s - \frac{3}{11} f_x \ . \tag{1}$$

The integrated differential Doppler, i.e., the differential phase δm_{sx}, is proportional to the change in the electron columnar density δN_T,

$$\delta m_{sx} = \int \delta f_{sx} \, \mathrm{d}t = 0.543 \delta N_T \ , \tag{2}$$

with

$$N_T = \int_U^{\oplus} n_e(s) \, \mathrm{d}s \ , \tag{3}$$

where $n_e(s)$ is the electron density along the downlink ray path s from *Ulysses* (U) to Earth ($\oplus$).

Differential Doppler measurements were recorded on a nearly continuous basis during the conjunctions C_1, and C_4. The raw data from the various ground stations, measurements of Doppler residuals, were sampled at $\delta t = 1$ s. Because the data were not always continuous, sometimes having gaps lasting from a few seconds to a few minutes, careful processing was necessary to remove poor data and to flag stretches with data gaps.

On numerous occasions, Doppler data were recorded simultaneously at different ground stations. During these limited opportunities it was possible to perform a cross-correlation analysis with the data from the two stations. The time lag of maximum correlation was assumed to be the time taken for the solar wind to move a distance equal to the radial projection (ΔR) of the actual spatial separation of the radio ray paths between the two ground stations and *Ulysses*. The definition of the distance ΔR is illustrated in Figure 1, a schematic representation of the relative positions of Sun and Earth (points S and E, respectively) and the *Ulysses* spacecraft during a radio sounding experiment. The solar offset of the radio ray path R is the distance from the center of the Sun (point S) to the solar proximate point B along the line-of-sight between Earth and *Ulysses*. Corresponding solar proximate points along the ray paths from *Ulysses* to two widely-separated ground stations are denoted A (Eastern receiving station) and C (Western receiving station). Indicated in the plane-of-sky view in Figure 1 (inset) are the actual spatial separation of the radio ray paths between points A and C (ΔS) and its radial projection (ΔR), which are computed from the known geometry for the date and time of the observations. Typical values for ΔS and ΔR are a few thousand km.

Wohlmuth *et al.* (1997) have also calculated correlation lag times to determine solar wind flow velocities with the *Ulysses* Doppler data from C_1. Rather than using separate downlinks at two ground stations, however, Wohlmuth *et al.* (1997) computed the cross-correlation between uplink and downlink at single stations. The typical coronal separation for the uplink/downlink correlations (10–20 thousand km) are considerably larger than for the two-station experiment.

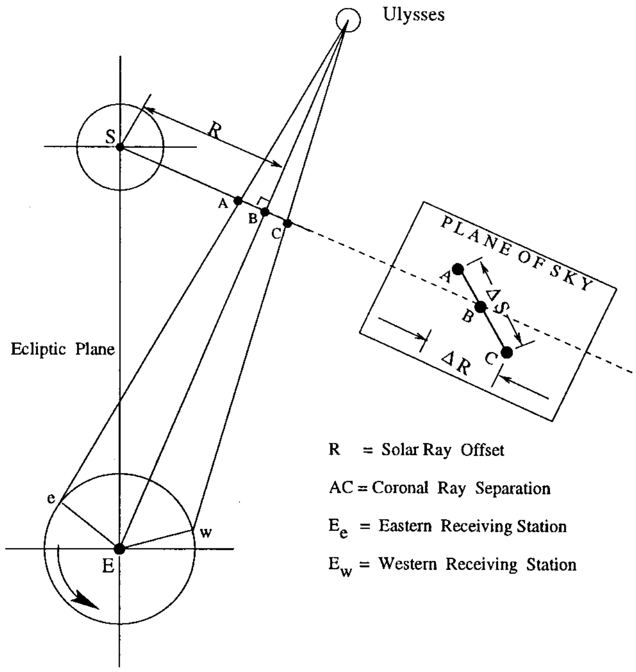

Figure 1. Schematic representation of the *Ulysses* SCE geometry. The relative positions of Sun (S), Earth (E), and *Ulysses* (U) form the sounding plane S–E–U. The solar offset of the radio ray path R is the distance between the points S and B. Indicated in the orthogonal plane-of-sky view (inset at right) is the actual spatial separation AC of the radio ray paths from the spacecraft to two ground stations on Earth (distance: ΔS). The projection of ΔS onto the solar radial is ΔR.

Another technique for determining plasma flow velocities at solar distances from 3–30 $R_\odot$ is photometric tracing of features in the white-light corona with the LASCO coronagraph on SOHO (Sheeley *et al.*, 1997). Rather than a correlation in time for a known coronal radial separation, the differenced images from LASCO basically yield the ΔR (and thus radial velocity) from two snapshots taken at precisely known times. As with the cross-correlation technique discussed here, it is essential to the observation that the corona be sufficiently structured to produce the necessary contrast in the white-light images. The LASCO measurements reported for the coronal streamer belt yield exceptionally accurate velocity profiles with distance from the Sun. Roughly constant acceleration was reported for the white-light 'leaves in the wind' from 150 km s^{-1} at 5 $R_\odot$ to 300 km s^{-1} at 25 $R_\odot$. The continuous monitoring of one and the same solar wind stream is a significant advantage over the radio correlation technique, which gathers random samples from many streams at isolated points in time and space.

Figure 2 is an example of the correlations obtained on 1 September 1991 (day of year, DOY = 244) between the DSN ground stations at Madrid (DSS 63) and Goldstone (DSS 14) during the conjunction C_1. The dashed and dotted curves

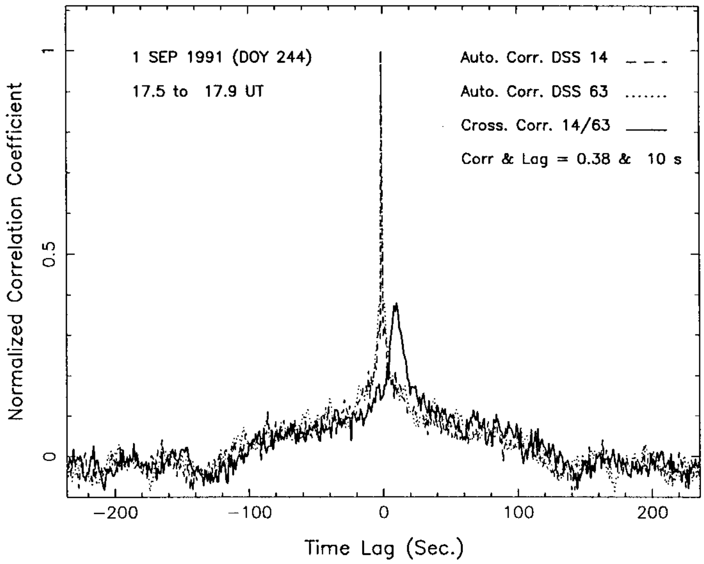

Figure 2. Correlations obtained on 1 September 1991 (day of year, DOY = 244) for ground stations at Madrid (DSS 63) and Goldstone (DSS 14) during conjunction C_1. The dashed and dotted curves are the autocorrelations. The solid curve is the cross correlation with a maximum value of 0.38 at time lag $\tau = 10$ s.

are the autocorrelation functions of the two data sets from DSS 63 and DSS 14, respectively. The solid curve is the cross-correlation function. Whereas the autocorrelations peak sharply at zero time lag, the cross correlation is seen to attain a maximum value of 0.38 at a time lag $\tau = 10$ s. It was observed that the cross-correlation coefficients for all the examples of two-station data during both C_1 and C_4 never exceeded 0.4. One reason for this was that the data were rather noisy when tracking a source so close to the Sun.

Figure 3 shows the raw data (upper panels) and the power spectra (lower panels) for the data corresponding to Figure 2. Data for the ground station DSS 63 are shown on the left; DSS 14 on the right. An appropriate number of zeros have been appended to the data in order to have a total of 2048 points (2^{11}) for use in standard Fast Fourier Transform (FFT) software. The spectra are plotted up to the Nyquist frequency $\nu_N = 0.5$ Hz and have been normalized to the highest spectral density. It is evident that the high frequency end of the spectrum (> 0.1 Hz) is dominated by system (receiver) noise which significantly degrades the cross correlations.

3. Improving the Two-Station Cross Correlations

In contrast to IPS spectra, which provide information at frequencies between 0.1 Hz and a few Hz, the propagation medium affects the Doppler sounding spectra at frequencies $0.001 < \nu \leq 0.1$ Hz. This implies that the scale sizes affecting the

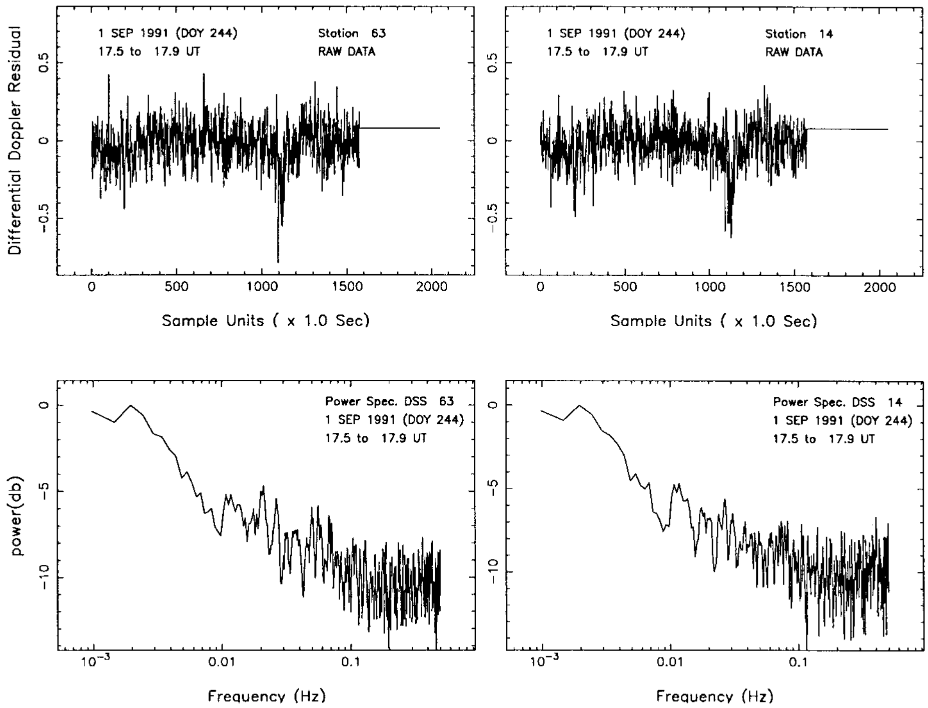

Figure 3. Raw data (upper panels) showing the differential Doppler residuals as a function of time and the normalized power spectra (lower panels) for the correlations shown in Figure 2 (*left*: DSS 63; *right*: DSS 14.) Note that the spectra are dominated by noise from 0.1 Hz up to the Nyquist frequency $\nu_N = 0.5$ Hz.

Doppler sounding data are typically 1–2 orders of magnitude greater than those probed by IPS. As seen from the spectra in Figure 3, receiver noise dominates beyond 0.1 Hz. This noise does not correlate between the two ground stations and hence degrades the cross correlations. Using an FFT to display the data in the frequency domain, the undesired high frequencies can be removed by suppressing spectral amplitudes above a cutoff frequency ν_c. The 'filtered' data, which can be recovered via an inverse FFT, yield cross-correlation coefficients that are significantly higher than those obtained from raw unfiltered data.

Figure 4 shows the data of DOY 244 for station 63 along with the corresponding power spectra after application of various degrees of filtering. Each pair of panels from the top show doppler residuals for station 63 (left panel) and the corresponding power spectra (right panel) after 60%, 75%, and 95% of the high frequencies have been removed. This filtering corresponds to removing all fluctuations at frequencies $\nu > \nu_c$, where ν_c is 0.200, 0.125 and 0.025 Hz, respectively. All the spectra feature steep dropouts beyond the frequency ν_c (indicated in each of the panels on the right by a vertical dashed line).

Figure 5 shows the correlations after the data have been filtered. The solid curve in each of the panels on the left shows the cross correlation; the dashed and dotted curves are the autocorrelation functions. It can be seen that successive stages of filtering steadily improves the correlation coefficient. The time lag of maximum correlation, on the other hand, remains more or less stable. The time lag and the amplitude of the correlation maximum were determined systematically by fitting 32 points around the peak of the correlation by a Gaussian. The centroid, amplitude and the width of the fitted Gaussian, as well as the formal errors in these values, were then calculated. The panels on the right in Figure 5 show these Gaussian fits around the peak of the cross correlation.

The noise in the Doppler data increases as the solar offset of the radio ray path to *Ulysses* decreases. Thus data at small solar offsets require more extensive filtering in order to achieve significantly large correlation coefficients. The filtering factor was set to the highest reasonable amount of 95% ($v_c = 0.025$ Hz) for uniformity in the data processing. This extreme level of filtering was possible because, as seen from many examples, the derived time lags were independent of the degree of filtering. Data sets that showed a correlation coefficient of less than 0.4 after filtering and those that gave values of time lag $\tau < 10$ s were dropped, as were a few data sets that yielded negative time lags. Out of a total of 39 sets of data during conjunction C_1, 19 sets were retained and used for further analysis. For conjunction C_4, data sets showing negative time lags and those with correlation coefficients less than 0.4 after filtering were dropped. From a total of 23 data sets, 16 were retained for further analysis. The weak correlation in the discarded data sets is attributed to a lack of significant electron density fluctuation amplitude in the propagation medium near the solar proximate point. If no ‘tracers’ are entrained in the outward flowing solar wind, then no discernable fluctuations will be imparted to the phase of the radio signals along the two ray paths.

4. Two-Station Coronal Velocities from C_1 and C_4

Figure 6 shows the measurements of solar wind velocity determined from two-station correlations during C_1. The velocity estimates (right scale: solid circles joined by a broken line) are plotted together with columnar electron density measurements obtained from *Ulysses* dual-frequency ranging data (Bird *et al.*, 1994). The columnar electron densities (left scale: small solid squares) are measured in hexems (1 hexem $= 10^{16}$ electrons m^{-2}). No velocity measurements were available between DOY 231 and DOY 236, as there were no simultaneous measurements available from ground stations during this period. The error in each time lag measurement was taken to be the sum of the half-width of the Gaussian fit to the correlation peak at the 95% point and the formal error in the mean value of the Gaussian fit. The vertical bars on each velocity measurement are $\pm$ this error. The upper panel in Figure 6 shows a scaled solar disk projection of the C_1 occultation

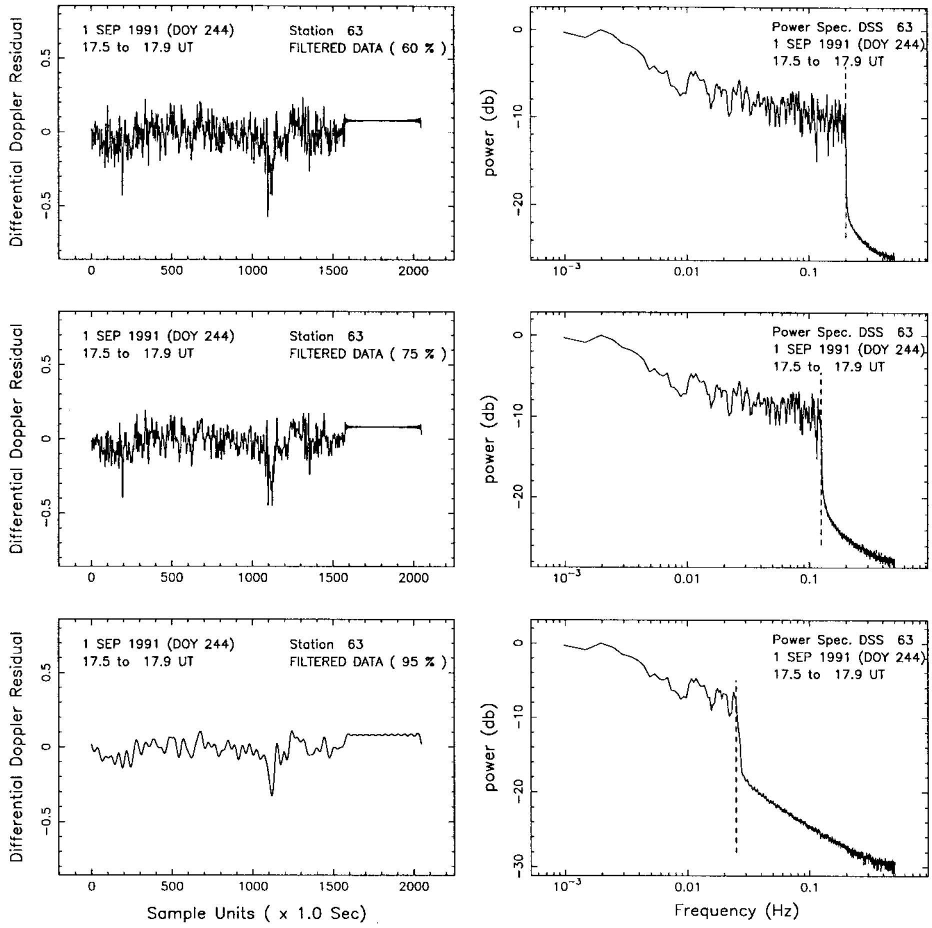

Figure 4. Each pair of panels starting from the top shows the Doppler residuals on DOY 244 for station 63 (*left panel*) and the corresponding power spectra (*right panel*) after removing 60%, 75% and 95% of the high frequencies, respectively. This filtering corresponds to removing all frequencies $\nu > \nu_c$, where ν_c (vertical dashed lines) is 0.200, 0.125, and 0.025 Hz, respectively.

geometry as *Ulysses* passed behind the Sun from east to west. The trajectory is marked by a straight line with the position of *Ulysses* shown by solid circles at 0 UT everyday. The solar offset distance of the ray path proximate point is indicated on the upper abscissa scale. The smallest solar offset distance reached by *Ulysses* was 4.3 $R_\odot$ on 21 August 1991. This event is marked by an arrow in both panels of Figure 6.

In contrast to the impressive velocity profiles of Sheeley *et al.* (1997), the 19 velocity measurements in Figure 6, derived from two-station correlations, do not display an obvious acceleration of the solar wind over the range of solar offset distances from 7 to 38 $R_\odot$. On the other hand, the velocity determinations from *Ulysses* uplink/downlink correlations (Wohlmuth *et al.*, 1997) clearly increase with

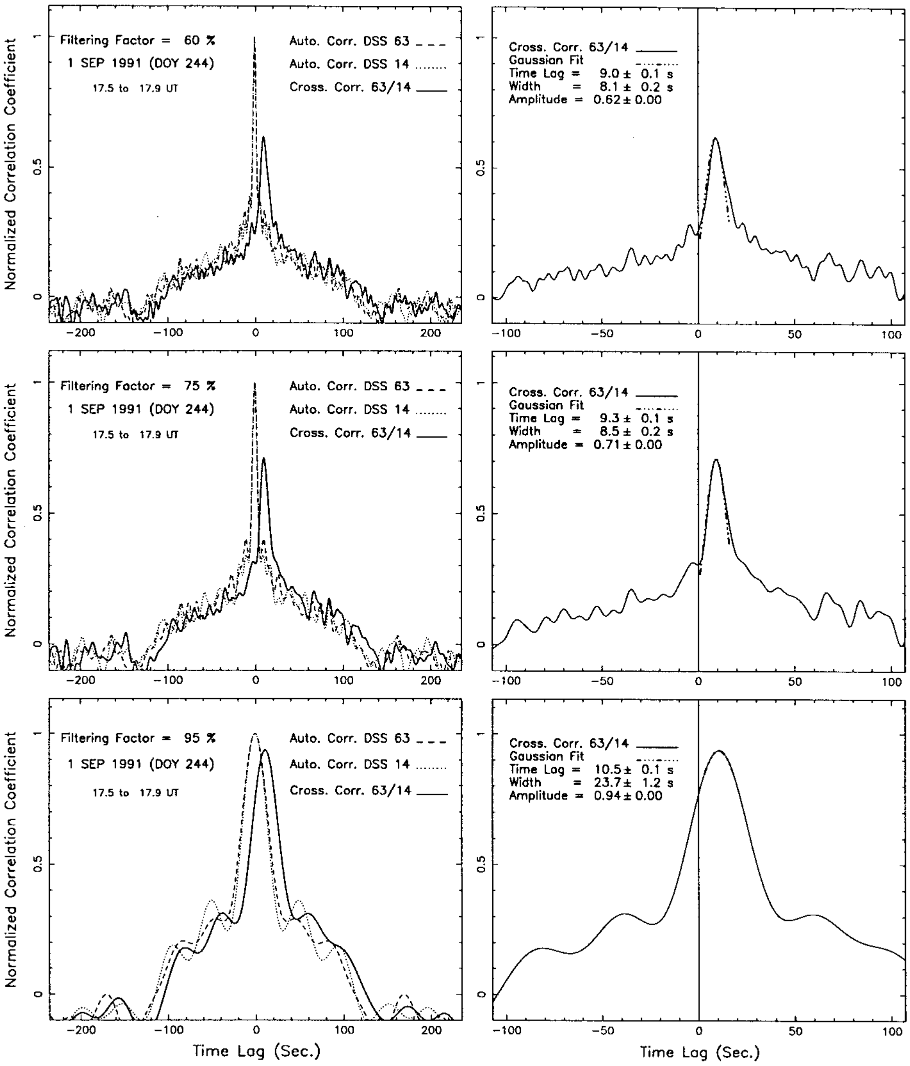

Figure 5. Autocorrelation and cross-correlation functions obtained after 60%, 75%, and 95% filtering (*left panels*), respectively. The panels on the right show slightly magnified plots of the cross correlation (solid line) with Gaussian fits to the data around the peak (superimposed dotted curves). The Gaussian fit parameters and formal errors in the fit procedure are indicated.

increasing solar distance. The apparent discepancy can be explained partially by projection effects and partially by the nonsimultaneous random sampling of the two-station and uplink/downlink measurements.

Another reason for the absence of a clear trend with solar offset is the mixture of high-speed and low-speed solar wind streams along the radio ray path. Pätzold *et al.* (1997) examined the *Ulysses* ranging data in detail and concluded that separate radial profiles existed for the electron density and solar wind velocity

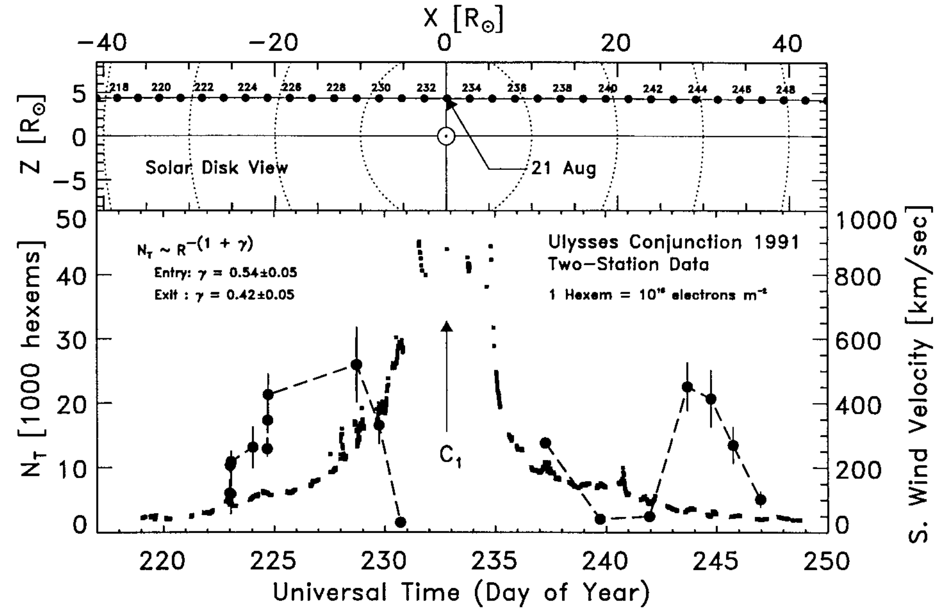

Figure 6. Measurements of columnar electron density (*left scale*: small solid squares) and solar wind velocity (*right scale*: solid circles) during C_1. The abscissa shows UT, represented as a 1991 day-of-year (DOY) number. The upper panel shows the occultation geometry (solar disk view) during C_1, correctly scaled in time with the lower diagram. The trajectory is marked by a straight line with the position of *Ulysses* shown by filled circles at 0 UT everyday. The solar offset distance is indicated by dotted concentric circles with radii in units of 10 $R_\odot$.

in coronal holes as opposed to regions within the streamer belt. At least beyond 60 $R_\odot$, observations from Helios (Schwenn *et al.*, 1978) first revealed the bimodal nature of the solar wind. The distinct contrast between these two modes and the associated dependence on heliolatitude was even more clearly demonstrated on *Ulysses* (Phillips *et al.*, 1994). The solar wind is either fast with low density or slow with high density. Moreover, much larger values of fractional electron density variations, which are important for the correlation, are found in the slow speed streams (Woo *et al.*, 1995). Nevertheless, large variations in the velocity estimates are found at similar solar offset distances, indicating that the random samples of correlation time lag are being dominated off and on by both fast and slow streams. In order to test whether the high density/low speed (and vice versa) trend persists in the young solar wind below 40 $R_\odot$, it was decided to examine the relationship between the velocity estimates and the *radially detrended* electron column density.

The columnar electron density $N_T(R)$, defined in Equation (3), was found to follow a radial power-law dependence with a single exponent given by $1 + \gamma$ (Pätzold *et al.*, 1992; Bird *et al.*, 1994). The slightly different values of γ for ingress and egress are indicated on the plot in Figure 6. It was shown (Bird *et al.*, 1994) that a good fit to the data could be obtained with

$$N_T(R) = K(\alpha) N_B R_\odot \left[\frac{R_\odot}{R}\right]^{\alpha-1} , \tag{4}$$

where N_B and $K(\alpha)$ are constants and $\alpha = \gamma + 2$ is the radial power-law exponent of the electron density. For a constant and radially symmetric solar wind expansion, $\gamma = 0$ and $\alpha = 2$. The value of the exponent α for C_1 was found to be $\alpha = 2.54$ and $\alpha = 2.42$ for ingress and egress, respectively, indicating that the solar wind was still accelerating in this range of solar distances ($4\ R_\odot < R < 40\ R_\odot$). Pätzold, Tsurutami, and Bird (1997) demonstrated that Equation (4) is not strictly valid for the case when the radio ray path passes through both coronal hole and coronal streamer regions along the limb. Different values of α hold in these regions and the asymptotic state with radial expansion at constant velocity is achieved at much smaller solar distances in coronal holes. Nevertheless, Equation (4) is considered to be quite adequate for the radial detrending procedure applied here.

Using the above indicated values of the radial falloff exponent α, the strong radial dependence of the electron density distribution can be removed and the extrapolated value of the electron content can be given at some chosen solar offset distance (say, 20 $R_\odot$). The technique of removing the radial dependence was utilized by Woo *et al.* (1995) to compute the fractional electron density fluctuations during C_1. However, no corresponding velocity measurements were analyzed in their work.

Figure 7 shows basically the same plot as Figure 6 (lower panel), except now the total electron content has been projected to 20 $R_\odot$ after compensating for the radial dependence from Equation (4). The radially detrended electron content (open triangles) is plotted on the left ordinate scale and solar wind velocity (filled circles with error bars) is plotted on the right ordinate scale. *In situ* plasma measurements outside 60 $R_\odot$ (e.g., Schwenn, 1990; Gosling *et al.*, 1981) have shown that the peaks in the density profiles follow the neutral line separating sector boundaries and are the apparent extensions of coronal streamers containing slow solar wind. Figure 7 shows that the same situation holds close to the Sun. Velocity minima appear at the same times as the peaks in the density profiles.

Figure 8 shows measurements of velocity and total electron content, derived from the conjunction C_4 (February–March 1995). Velocity measurements are plotted on the right ordinate scale with each measurement shown by an open diamond joined by a broken line. The ranging measurements of total electron content are plotted on the left ordinate scale in hexems. Each individual 5-minute range measurement is shown by a small filled square. The data gaps in the ranging measurements are due to incomplete tracking coverage at the various ground stations. The heliographic latitude of the solar proximate point is plotted on the upper abscissa scale. All of the high velocities are confined to the polar regions above 60° S and the low velocities are all at latitudes below 60°. The electron content peaks in the streamer belt at a latitude of $\backsimeq$ 20° and reaches its minimum over the coronal hole dominated southern polar regions. The large velocities and correspondingly large

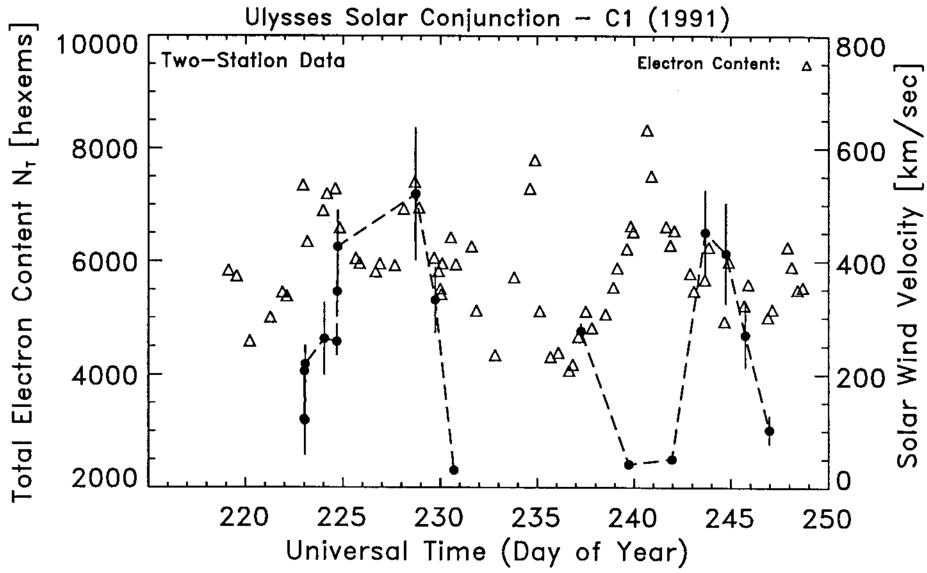

Figure 7. Radially detrended columnar electron content (open triangles) and solar wind velocity measurements (solid circles) during C_1. This plot is similar to Figure 6, but the total electron content has been extrapolated to 20 $R_\odot$ from the radial dependence given by Equation (4).

errors measured over the polar regions of the Sun are probably due to the unusual occulting geometry with significant nonradial alignment of the radio ray paths to the two ground stations during the tracking passes.

5. Discussion and Conclusion

In the entire analysis, the time associated with each velocity estimate was arbitrarily taken to be the time corresponding to the midpoint of the data interval used for the cross correlation and the value of the radial projection ΔR was computed for that time. However, ΔR changes continuously with time and can be different from the assumed value even within the approximately 35 min corresponding to the data length.

Figure 9 shows how the coronal ray path separation changes with time for a few pairs of ground stations during occultation C_1. The thick and thin lines represent the ray path separations ΔS and ΔR (see Figure 1) for the specific pairs of ground stations as indicated in the plot. The thin vertical lines denote the times of the mid-points of four two-station measurement intervals (each with 2048 Doppler measurements at 1 sample s^{-1}). In the case of the Goldstone/Canberra observations of DOY 224 shown in Figure 9, the decrease in ΔR is about 400 km over the duration of the measurement. This represents a 10% error in the assumed value of ΔR.

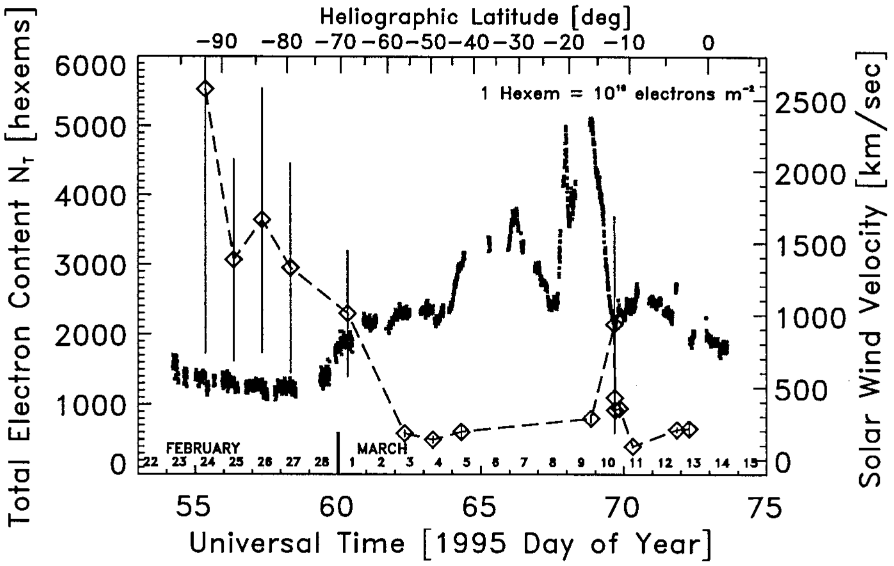

Figure 8. Velocity measurements derived from two-station correlations compared with electron content measurements during conjunction C_4 in February–March 1995. The velocities (diamonds with error bars joined by a broken line) are plotted on the right ordinate scale; the electron content in hexems (small solid squares) on the left. The heliographic latitude of the solar proximate point is plotted on the upper abscissa.

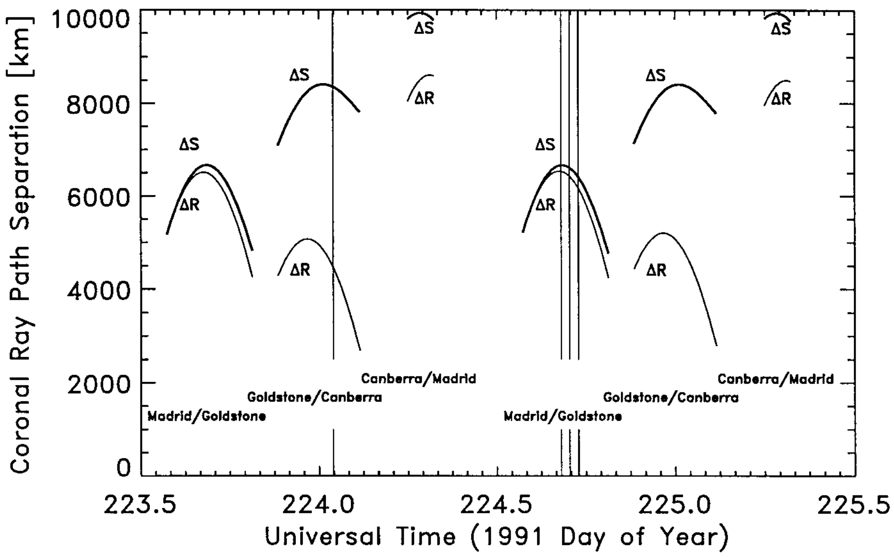

Figure 9. Coronal ray path separation during a time segment during C_1. Each pair of thick and thin solid lines are the ray path separations ΔS and ΔR respectively, for the specific pairs of ground stations indicated in the plot. The four thin vertical lines denote times corresponding to the mid-points of the data intervals (duration: 2048 s) for which velocity estimates were made.

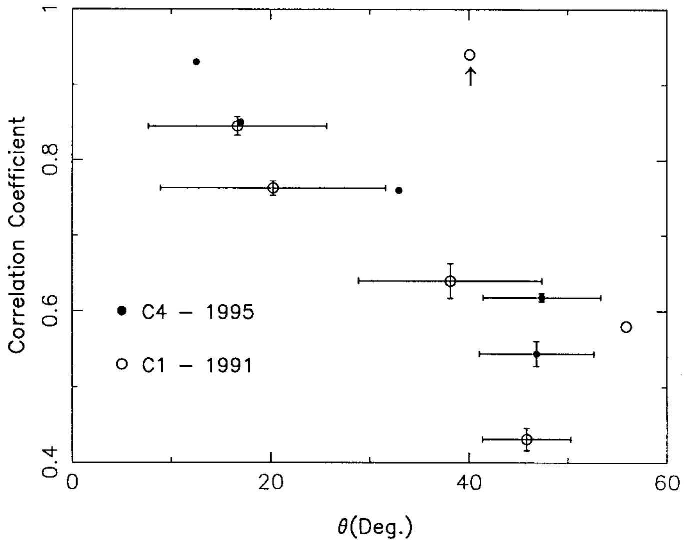

Figure 10. Two-station correlation coefficient as a function of the angle θ between ΔR and ΔS. Each point is the average of all data in bins of 0.1 in correlation coefficient. Standard 1σ bars indicate the spread in correlation coefficient and angle θ for all bins containing more than one point. The open (solid) circles are from conjunction C_1 (C_4). The singular point corresponding to DOY 244, when the solar wind was particularly structured, is marked by a small vertical arrow.

A more serious error is associated with the nonradial alignment of the ray paths to the two ground stations. For conjunction C_4, the occultation geometry was such that ΔR sometimes reduced to less than 5% of ΔS. This resulted in large velocity and error estimates at high latitudes during C_4 when the ray paths were over the polar regions.

Figure 10 shows a scatter plot of the correlation coefficient as a function of the angle θ between ΔR and ΔS. Each point plotted is the average of all data in bins of 0.1 in correlation coefficient. Standard 1σ bars indicate the spread in correlation coefficient and angle θ for all bins containing more than one point. The conjunctions C_1, and C_4 are shown in Figure 10 by open and filled circles, respectively. It can be seen from Figure 10 that when the correlation coefficient is high, the radial alignment between the ray paths is generally good with the angle θ between ΔR and ΔS being small. Since Doppler sounding observations reported here are sensitive to scale sizes of a few thousand kilometers, the correlation is expected to be degraded when the lateral (nonradial) displacement between the ray paths is greater than several thousand kilometers. This effect becomes evident in Figure 10 for $\theta > 30°$. Exceptions to this trend occur when the solar wind plasma is highly structured, as in the case of DOY 244 (see Figures 2–6). The point corresponding to this day is marked in Figure 10 by a small vertical arrow.

In conclusion, Fourier filtering of the Doppler sounding data by the method described in this paper is effective in enhancing cross-correlation coefficients and can be used in deriving coronal velocities in the distance range 4 $R_\odot$ to 40 $R_\odot$. The 2-station velocities measured during conjunctions C_1 and C_4 displayed the trend observed by *in-situ* observations outside 60 $R_\odot$: high velocities associated with regions of low total electron content and vice versa. Since the peaks in the density profiles are known to follow the neutral line, whose northward and southward extensions essentially define the streamer belt of low solar wind velocity, it was not unexpected that the velocity estimates are generally lower in regions of relatively high total electron content.

Acknowledgements

One of the authors (PJ), would like to acknowledge support from a Humboldt Research Award in 1996−1997, during which this work was carried out. Parts of this work were performed at the Jet Propulsion Laboratory (JPL), California Institute of Technology, under a contract with NASA. The *Ulysses* SCE observations were made with the radio antennas of the NASA Deep Space Network with support of the Multimission Radio Science Support Team at JPL. This work was supported in part by the Deutsches Zentrum für Luft- und Raumfahrt (DLR) under grants 50 ON 9104 and 50 ON 9401.

References

Ananthakrishnan, S., Balasubramanian, V., and Janardhan, P.: 1995, *Space Sci. Rev.* **72**, 229.

Bird, M. K.: 1982, *Space Sci. Rev.* **33**, 99.

Bird, M. K. and Edenhofer, P.: 1990, in R. Schwenn and E. Marsch (eds.), *Physics of the Inner Heliosphere 1*, Springer-Verlag, Heidelberg, p. 13.

Bird, M. K., Asmar, S. W., Brenkle, J. P., Edenhofer, P., Pätzold, M., and Volland, H.: 1992, *Astron. Astrophys. Suppl. Ser.* **92**, 425.

Bird, M. K., Volland, H., Pätzold, M., Edenhofer, P., Asmar, S. W., and Brenkle, J. P.: 1994, *Astrophys. J.* **426**, 373.

Bird, M. K., Pätzold, M., Edenhofer, P., Asmar, S. W., and McElrath T. P.: 1996, *Astron. Astrophys.* **316**, 441.

Coles, W. A. and Maagoe, S.: 1972, *J. Geophys. Res.* **77**, 5622.

Dennison, P. A. and Hewish, A.: 1967, *Nature* **213**, 343.

Efimov, A. I., Yakovlev, O. I., Shtrykov, V. K., Rogalskii, V. I., and Tikhonov, V. F.: 1981, *Soviet Radio Engg. Elec.* **26**, 311.

Gosling, J. T., Borrini, G., Asbridge, S. J., Bame, W. C., Feldman, W. C., and Hansen, R. T.: 1981, *J. Geophys. Res.* **86**, 5438.

Hewish, A. and Symonds, M. D.: 1969, *Planetary Space Sci.* **17**, 313.

Hewish, A. and Wyndham, J. D.: 1963, *Monthly Notices Royal Astron. Soc.* **126**, 649.

Hewish, A., Scott, P. F., and Wills, D.: 1964, *Nature* **203**, 1214.

Jackson, B. V.: 1991, in E. Marsch and R. Schwenn (eds.), *Solar Wind Seven*, Pergamon, Oxford, p. 623.

Janardhan, P., Balasubramanian, V., Ananthakrishnan, S., Dryer, M., Bhatnagar, A., and McIntosh, P. S.: 1996, *Solar Phys.* **166**, 379.

Kakinuma, T., Washimi, H., and Kojima, M.: 1973, *Publ. Astron. Soc. Japan* **25**, 271.

Manoharan, P. K., Ananthakrishnan, S., Dryer, M., Detman, T. R., Leinbach, H., Kojima, M., Watanabe, T., and Kahn, J.: 1995, *Solar Phys.* **156**, 377.

Pätzold, M., Tsurutani, B. T., and Bird, M. K.: 1997, *J. Geophys. Res.* **102**, 24151.

Pätzold, M., Bird, M. K., Volland, H., Edenhofer, P., Asmar, S. W., Brenkle, J. P.: 1992, in R. Schwenn and E. Marsch (eds.), *Solar Wind Seven*, Pergamon, Oxford, p. 237.

Pätzold, M., Bird, M. K., Edenhofer, P., Asmar, S. W., and McElrath, T. P.: 1995, *Geophys. Res. Letters* **22**, 3313.

Phillips, J. L., Balogh, A., Bame, S. J., Goldstein, B. E., Gosling, J. T., Hoeksema, J. T., McComas, D. J., Neugebauer, M., Sheeley, N. R, Jr., and Wang, Y.-M.: 1994, *J. Geophys. Res. Letters*, 1105.

Rickett, B. J. and Coles, W. A.: 1991, *J. Geophys. Res.* **96**, 1991.

Schwenn, R.: 1990, in R. Schwenn and E. Marsch (eds.), *Physics of the Inner Heliosphere 1*, Springer-Verlag, Heidelberg, p. 99.

Schwenn R., Montgomery, M. D., Rosenbauer, H., Miggenrieder, H., Mühlhäuser, K. H., Bame, S. J., Feldman, W. C., and Hansen, R. T.: 1978, *J. Geophys. Res.* **83**, 1011.

Sheeley, Jr., N. R., Wang, Y.-M., Hawley, S. H., Brueckner, G. E., Dere, K. P., Howard, R. A., Koomen, M. J., Korendyke, C. M., Michels, D. J., Paswaters, S. E., Socker, D. G., St. Cyr, O. C., Wang, D., Lamy, P. L., Zulebaria, A., Schwenn, R., Simnett, G. M., Pluskett, S., and Biesecker, D. A.: 1997, *Astrophys. J.* **484**, 472.

Tyler, G. L., Vesecky, J. F., Plume, M. A., and Howard, H. T.: 1981, *Astrophys. J.* **249**, 318.

Wohlmuth, R., Plettemeier, D., Edenhofer, P., Bird, M. K., Pätzold, M., and Asmar, S. W.: 1997, *Radio Sci.* **32**, 617.

Woo, R. and Armstrong, J. W.: 1981, *Nature* **292**, 608.

Woo, R., Armstrong, J. W., Sheeley N. R., Jr., Howard, R. A., Michels, D. J., and Koomen, M. J.: 1982, *Nature* **300**, 157.

Woo, R., Armstrong, J. W., Bird, M. K., and Pätzold, M.: 1995, *Geophys. Res. Letters* **22**, 329.

Yakovlev, O. I., Efirnov, A. I., Razmanov, V. M., and Shtrykov, V. K.: 1980, *Soviet Astron.* **24**, 454.